

Preliminary Steps in Assimilating SSM/I Brightness Temperatures in  
a Hurricane Prediction Scheme

C. Amerault and X. Zou

Florida State University, Tallahassee, FL

Revised December 2002

# Abstract

Different aspects of assimilating satellite observed microwave radiances (brightness temperatures) into the initial vortex of a hurricane prediction model are discussed. The tangent linear and adjoint observation operators were developed from a computationally inexpensive and reasonably accurate radiative transfer model. These models have the advantage of being able to perform in all types of weather, including rain. The adjoint radiative transfer model was used to conduct a sensitivity analysis of brightness temperatures to different atmospheric and surface variables. The sensitivities computed by the model compare favorably with physical understandings of how brightness temperatures are affected by the atmosphere and the surface. The errors associated with some of the approximations in the radiative transfer model were estimated from comparisons with a more accurate model. These errors were found to be smaller than estimates from previous studies. The random errors associated with brightness temperature observations were also estimated from statistical structure function calculations and were found to be in line with estimates previously used. The models developed and the errors calculated for this study will be used in future work to assimilate brightness temperatures in hurricane initializations and to evaluate the performance of different microphysical schemes in hurricane prediction.

# 1 Introduction

Passive microwave remote sensing provides invaluable information on meteorological quantities such as precipitation, specific humidity, and surface ocean wind speeds. However, microwave-sensing instruments such as the Special Sensor Microwave/Imager (SSM/I) only measure radiances, or brightness temperatures ( $T_b$ s), which are indirectly related to the quantities used in Numerical Weather Prediction (NWP) models. Unlike conventional observations, such as temperature and pressure,  $T_b$ s cannot be directly assimilated into NWP models. Early use of SSM/I observations focused on the retrieval of conventional variables from radiances through empirical regression algorithms (Hollinger 1991). Unfortunately, these methods often cannot account for the nonlinear interactions between  $T_b$ s and the atmospheric state, especially in the presence of hydrometeors. Instead of using retrieved products, Eyre et al. (1993) proposed a method where satellite radiances could be utilized in a more direct manner. The basis of this method is a variational assimilation scheme which maps conventional meteorological variables into satellite radiance space using a radiative transfer model (RTM). Phalippou (1996) extended this method to SSM/I observations in order to retrieve humidity profiles, cloud liquid water paths, and surface wind speeds over the ocean. In both studies, the retrieval could only be applied in rain-free areas because the RTM was unable to incorporate precipitation information. Aonashi and Liu (1999) studied the impact of using variational retrieval in mesoscale disturbances by using a RTM developed by Liu (1998) which included hydrometeors (both liquid and ice). All of these studies saw a positive impact on NWP forecasts using the quantities retrieved from the variational scheme. However, they all required a great amount of computational time in order to calculate the gradient of the  $T_b$ s with respect to conventional meteorological variables (a requirement of the variational scheme) because a perturbation method was used for this calculation. Zou et al. (2001) developed an adjoint RTM which

allowed for much faster calculations of this gradient. However, the model used in Zou et al. (2001) was similar to the model used by Eyre et al. (1993) and Phalippou (1996) so the method could only be used in precipitation-free environments. Still, improvements in the forecast of a tropical system were realized by assimilating  $T_b$ s surrounding the storm.

In this present study, the adjoint of Liu's (1998) RTM is developed in an effort to eventually assimilate  $T_b$ s in areas where there are a large number of hydrometeors, i.e. in the middle of a storm. The adjoint RTM is used for a sensitivity analysis to determine which model fields are most influential in radiative transfer calculations.

In order to assimilate radiances in a variational framework, information on the errors associated with the observations are necessary. There are two types of errors that need to be determined when using  $T_b$ s. The first is the error associated with the actual  $T_b$  observations. These measurements are assumed to be unbiased, and previous studies using SSM/I  $T_b$ s (Phalippou 1996; Aonashi and Liu 1999) have used the radiometric sensitivities of the SSM/I as estimates of the observational error variances. This study will further examine the observational error variances through the use of structure functions.

The second type of error is that which results from the radiative transfer calculations. There are many sources of error associated with the RTM. Here, we will quantify the error due to an approximation in the radiative transfer calculations that improves the speed of the RTM. However there are other, potentially larger, sources of error that exist especially when the model is used in rainy conditions. The source of these errors as well as their possible estimates will also be discussed.

Section 2 reviews the variational method used for assimilating  $T_b$ s proposed by Eyre et al. (1993) as well as the SSM/I microwave radiance observations used in this study. Section 3 will briefly touch on the bogus data assimilation (BDA) scheme (Zou and Xiao 2000) which was used

to create the NWP model fields used in this study. Section 4 highlights results from adjoint sensitivity analyses, and Section 5 investigates the errors associated with both the observations and the RTM. A summary as well as a discussion of work planned for the future will be discussed in Section 6.

## 2 Variational Assimilation and SSM/I Observations

### 2.1 Variational Assimilation of Brightness Temperatures

The variational assimilation method proposed by Le Dimet and Talagrand (1986) and utilized by Eyre et al. (1993) to include satellite observed radiances, minimizes the value of a scalar cost function

$$J(\mathbf{x}) = \frac{1}{2}(H(\mathbf{x}) - \mathbf{y}^{obs})^T(\mathbf{O} + \mathbf{F})^{-1}(H(\mathbf{x}) - \mathbf{y}^{obs}) + \frac{1}{2}(\mathbf{x} - \mathbf{x}^b)^T\mathbf{B}^{-1}(\mathbf{x} - \mathbf{x}^b) \quad (1)$$

where  $\mathbf{x}$  is a state vector composed of atmospheric and surface variables and  $\mathbf{x}^b$  is a background vector usually composed of values taken from a previous forecast. The observed  $T_b$ s are contained in  $\mathbf{y}^{obs}$  and  $H$  is the RTM which computes  $T_b$ s from the input values of the atmospheric state in  $\mathbf{x}$ .  $\mathbf{O}$  is the estimated error covariance of the  $T_b$  observations,  $\mathbf{F}$  is the estimated error covariance of the RTM, and  $\mathbf{B}$  is the estimated error covariance of the background field.

The variational scheme is an attractive method because it includes both *a priori* information,  $\mathbf{x}^b$ , and error characteristics,  $\mathbf{O}$ ,  $\mathbf{F}$ , and  $\mathbf{B}$ , whose inverses serve as weightings. In order to assimilate a new type of observation such as SSM/I microwave radiances,  $\mathbf{H}$ ,  $\mathbf{O}$ , and  $\mathbf{F}$  need to be defined. The error information which is contained in  $\mathbf{O}$  and  $\mathbf{F}$  is discussed in section 5. Liu's (1998) RTM, which utilizes the discrete ordinate method with 4-streams for radiative transfer calculations (Liou 1974) is used as the observation operator  $\mathbf{H}$ . The 4-stream RTM computes a  $T_b$  for any microwave frequency based on the atmospheric temperature  $T$ , pressure,  $p$ , relative

humidity, cloud water  $q_c$ , rain water  $q_r$ , cloud ice  $q_{ci}$ , and snow ice  $q_s$ , as well as the surface temperature  $T_g$ , and the surface wind speed (only used over oceans).

In order to find the best estimate of  $\mathbf{x}$  which minimizes the value of  $J(\mathbf{x})$ , the gradient of  $J(\mathbf{x})$  is needed. The gradient of the cost function is obtained by differentiating (1) with respect to  $\mathbf{x}$ :

$$\nabla J(\mathbf{x}) = \mathbf{H}^T(\mathbf{O} + \mathbf{F})^{-1}(H(\mathbf{x}) - \mathbf{y}^{obs}) + \mathbf{B}^{-1}(\mathbf{x} - \mathbf{x}^b), \quad (2)$$

where

$$\mathbf{H} = \frac{\partial H(\mathbf{x})}{\partial \mathbf{x}} \quad (3)$$

is the tangent linear operator of the RTM.

To obtain  $\nabla J(\mathbf{x})$ , the gradient of the observation operator with respect to the control variables, the tangent linear operator  $\mathbf{H}$  and the adjoint operator  $\mathbf{H}^T$  are also needed. Since the calculation of  $T_b$ s is a one-dimensional problem (the  $T_b$  value at a specified point depends only on the vertical atmospheric profile and the surface conditions at that point) previous studies (Eyre et al. 1993; Phalippou 1996; Aonashi and Liu 1999) have used a simple perturbation method to approximate this gradient. This method entails slightly perturbing each input variable to the RTM separately and then running the RTM in order to calculate the gradient. The computational expense of this method is directly related to the number of levels in the RTM and the number of  $T_b$ s that need to be calculated, so that the expense can become relatively large as these factors grow. An adjoint RTM is an alternative and efficient tool for gradient calculations. Using an adjoint model requires only two model integrations (one forward model run and one adjoint model run) to calculate the gradient with respect to all input parameters. The tangent linear and adjoint models of Liu's (1998) RTM have been developed and tested in order to efficiently calculate  $\mathbf{H}$  and  $\mathbf{H}^T$ .

## **2.2 SSM/I Microwave Radiance Observations for Hurricane Bonnie (1998)**

The SSM/I is a seven channel passive radiometer which is part of the payload on polar orbiting Defense Meteorological Satellite Program (DMSP) satellites (Hollinger et al. 1987). Both vertical and horizontal polarizations are observed at 19.350, 37.000, and 85.500 GHz, (channels 19V, 19H, 37V, 37H, 85V, and 85H) while only vertically polarized measurements are recorded at 22.235 GHz (channel 22V). The resolution of the 85 GHz observations is roughly 15 km while the observations at all other channels have a coarser resolution of 60 km.

Hurricane Bonnie (1998) was chosen as the tropical cyclone of interest for this study. Bonnie reached hurricane strength on 22 August 1998 at 0600 UTC over the tropical Atlantic Ocean. Bonnie achieved its maximum strength on 23 August at 1200 UTC as a category 3 hurricane with a minimum central sea level pressure (SLP) of 954 mb and maximum surface winds of 100 kts. It then weakened slightly before making landfall in Wilmington, North Carolina on 27 August.

SSM/I observations from three DMSP satellites (F11, F13, F14) were made available over an 11 day period (19 - 29 August 1998) for this study. Two swaths over the tropical Atlantic Ocean for each satellite were provided daily (one at approximately 0000 UTC and the other at approximately 1200 UTC).

## **3 The Bogus Data Assimilation Scheme**

### **3.1 Overview of Bogus Data Assimilation**

The goal of this study is to investigate the properties of  $T_b$ s in hurricane environments. However, it is often difficult to reproduce such an environment in NWP fields from large scale analyses.

There are not enough quality observations in hurricane regions to fully resolve the structures of the initial vortex with the right position, intensity, and size of an actual hurricane.

The variational BDA scheme has been found to be a promising method for producing a dynamically consistent and conceptually correct initial vortex for hurricane prediction (Zou and Xiao 2000; Zou et al. 2001). The BDA scheme assimilates a bogused sea level pressure (SLP) field, which is generated from a few observed parameters, in a four-dimensional variational data assimilation (4D-Var) framework. Actual observations such as SSM/I radiances can be incorporated into the BDA procedure.

### **3.2 Producing the Initial Fields**

Seven bogus SLP fields were created at 12 hr intervals from 0000 UTC 22 to 0000 UTC 25 August 1998. 4D-Var was performed for each of the seven initial times using the MM5 (the fifth generation Penn State / NCAR Mesoscale Model; Dudhia et al. 1993) Adjoint Modeling System (Zou et al. 1997). The bogus SLP field was fitted to the original analysis in three minute intervals during a 30 minute assimilation window and was assumed to remain constant during the assimilation. All model state variables (i.e., pressure, temperature, wind, mixing ratio, etc.) adjusted to produce a surface low which was similar to the bogused low, while satisfying the dynamical and physical constraint provided by the MM5.

Each BDA field was created on 49x49 horizontal grid (30 km resolution) with 27 vertical levels. The BDA fields were then placed on larger grids (69X69X27 grid points) of the same resolution. Version 2 of the MM5 was run over the larger domain to create 12 hr forecast fields. Grell's cumulus parameterization, along with the Blackadar planetary boundary layer scheme and the Goddard explicit moisture scheme were used in the model integrations. The 12 hr

forecast fields created by the combination of BDA and the MM5 model integrations were used as input for the RTM.

### 3.3 BDA Results

The initial average track error for the seven forecasts was 23 km (within one model grid space of the actual hurricane center). By six hours, the track errors had increased to 67 km and at the twelve hour mark the average track error had only risen to 68 km. The average magnitude of the difference in the observed and forecasted minimum central SLP were 3, 7, and 11 mb for the initial, 6 hr, and 12 hr forecast times, respectively. The differences were generally less than 10 mb in magnitude except for the first two forecast periods (beginning 0000 and 1200 UTC 22 August) when Bonnie was rapidly developing. The average magnitudes of the difference in the forecasted and observed maximum winds were 47, 11, and 13 kts for the initial, 6 hr, and 12 hr forecast times. The greatest wind errors (as large as 60 kts) occurred at the initial time of each of the seven 12 hr forecasts because the BDA scheme was unable to fully correct the winds from the large scale analysis. By the sixth forecast hour the wind differences were generally less than 20 kts as the model had adjusted the wind field to the pressure field.

The observed  $T_b$ s and those calculated from the 12 hr forecast ending 0000 UTC August 25 for the 19V and 85V channels are shown in Figures 1 and 2. The observed and calculated 19V  $T_b$ s compare quite well in both the general pattern and the difference in values. The warmest  $T_b$ s are on the eastern side of the storm in both the observations and the forecast, indicating heavier precipitation (Section 4) to the east of the eye (the eye is located at 26.9°N 73.2°W). The difference between the forecasted and observed  $T_b$ s is generally less than 40 K.

The differences between the observed and forecasted  $T_b$ s in the 85V channel are much worse than in the 19V channel (Figure 2). The difference between the forecast and observations is

greater than 100 K just to the northeast of the eye, which is in the same area of the greatest model produced snow ice concentrations (not shown). As is seen in Section 4, the calculated  $T_b$  for the 85 GHz channels is extremely sensitive to the snow ice concentration, which means that more accurate hydrometeor concentrations, especially snow ice, could reduce this large difference between the forecasted and observed  $T_b$ s. Also, the RTM uses a Marshall Palmer distribution for ice particles and assumes that each ice particle is spherical. This is not necessarily how frozen hydrometeors are distributed or shaped in the real atmosphere, meaning that the assumptions in the RTM account for some of this difference as well.

Furthermore, the resolution of the model also plays an important role in accounting for the difference between the observed and forecasted  $T_b$ s at all channels. Even if the model is correctly predicting the hydrometeor fields at 30 km resolution, there is variability in the observed hydrometeor fields on much smaller scales (1-10 km) that will have a considerable effect on the  $T_b$  observations that will not be seen in the forecasted  $T_b$ s if the hydrometeor fields are assumed homogeneous over the model grid space, as is done in the RTM. This can lead to differences on the order of 10's of K (Kummerow et al. 1996). More discussion on these errors is provided in Section 5.2.3. In future work,  $T_b$  observations will be used to evaluate the performance of different explicit moisture schemes on smaller grid spacings.

## 4 Adjoint Sensitivity of the Radiative Transfer Model

### 4.1 Formulation

There are a number of ways to determine the sensitivity of a model. Traditional sensitivity analyses involve perturbing a few input parameters of a model and measuring the change in the response of the model. Adjoint models allow for the efficient calculation of the sensitivity of

a single response of a model to all the input parameters of the model. More recently, adjoint models have been used in data assimilation problems to determine the sensitivity of the optimal solution of the problem to the input parameters of the model (Zupanski 1995). For this study, an adjoint sensitivity analysis is performed, whereby the sensitivity of the  $T_b$  calculated by the RTM to the input of the RTM will be determined. In the case of the RTM, the response function is defined as

$$J_\alpha(\mathbf{x}) = T_b(\alpha), \quad (4)$$

where  $T_b(\alpha)$  is the  $T_b$  in the  $\alpha^{th}$  channel and  $\mathbf{x}$  is a vector which contains values of atmospheric and surface variables used as input for the RTM: air temperature, pressure, mixing ratio, cloud water, rain water, cloud ice, snow ice, ground temperature, and the sea surface wind speed. The sensitivity of  $J_\alpha$  with respect to  $\mathbf{x}$  is defined as

$$J_\alpha^{sens} = (\nabla J_\alpha)^T \delta \mathbf{x} = (\hat{\mathbf{x}})^T \delta \mathbf{x} \quad (5)$$

where  $\delta \mathbf{x}$  is a perturbation to the original input vector and  $\hat{\mathbf{x}}$  is the result of the adjoint model integration with a unit input for the adjoint variable for the  $\alpha^{th}$  channel and zero input for all other channels. The sensitivity of the response function to the  $l$ -th element of  $\mathbf{x}$  is expressed as

$$J_\alpha^{sens-l} = \hat{x}^l \delta x^l \quad (6)$$

The non-dimensional relative sensitivity  $S_\alpha^l$  (Zou et al. 1993) is defined as

$$S_\alpha^l = \frac{J_\alpha^{sens-l}}{J_\alpha} \left( \frac{\delta x^l}{x^l} \right)^{-1} = \frac{(\nabla J_\alpha)^l x^l}{J_\alpha} \quad (7)$$

The magnitude of the relative sensitivity serves as a guide to ranking the relative importance of the different components of the input vector in the computation of the  $T_b$  at a selected channel. A vertical profile of the relative sensitivity of the  $T_b$  to the input variables indicates which variables have the biggest effect on the  $T_b$ s and at what levels the effects are greatest.

## 4.2 Numerical Results

Average relative sensitivities were computed for three different types of atmospheric conditions: clear, rainy, and cloudy. Each grid point from the seven 12 hr MM5 forecasts was placed into one of these categories based on the following criteria. If the integrated rain water exceeded 1.0 mm or the integrated snow ice was greater than 0.5 mm at the grid point then it was considered rainy. These thresholds were obtained by noting that areas of large  $T_b$  depressions at 85 GHz coincided well with the respective threshold contours for integrated rain water and snow ice. For all points that were not rainy, if the integrated cloud water was greater than 0.1 mm then it was placed in the cloudy category. The cloudy threshold was determined by noting that areas of large  $T_b$  excesses at 19 GHz coincided well with the threshold contour of integrated cloud water. All other grid points which did not meet the requirements to be either rainy or cloudy were considered clear. From each category, 49 grid points were picked at random and the sensitivities were computed for the profile at each point and then the average was computed for each of the three weather conditions. The average profiles of the moisture variables for each weather condition is shown in Figure 3, the standard deviations are given by the horizontal bars. In clear conditions there are very few hydrometeors of any kind. In cloudy conditions there is a maximum  $q_c$  (cloud water) concentration of 0.25 g/kg located at 850 mb, and a small amount of  $q_r$  (rain water) is present in the lower levels. In rainy conditions, the  $q_r$  concentration is greatest (0.7 g/kg) from the surface up to 700 mb. The maximum  $q_c$  concentration is higher (at 500 mb) than the maximum in cloudy conditions, and the  $q_s$  (snow ice) concentration is greatest at 300 mb (0.75 g/kg), while the  $q_{ci}$  (cloud ice) concentration is much smaller (0.1 g/kg) and located slightly higher at 250 mb. As would be expected, the profiles of  $q$  (mixing ratio) show that the rainy points were the most moist while the clear points were the driest. The average temperature (not shown) in the lower atmosphere is warmest in clear conditions and coolest

in rainy condition, but the difference in the mean temperature between the different weather conditions is less than 1 K at every level. Above 600 mb, the rainy atmosphere is as much as 4 K warmer than the clear atmosphere and 3 K warmer than the cloudy atmosphere.

The average relative sensitivities for three channels (19H, 19V, and 85V) are shown in Figures 4-6. Only the largest atmospheric sensitivities (left hand plots) are displayed here. For clear conditions the sensitivities to  $T$  and  $q$  are larger than to other variables, for rainy conditions, the sensitivities to  $T$  and  $q_s$  are greater than to other variables, and in cloudy conditions, the sensitivities to  $T$ ,  $q$ , and  $q_c$  are greatest. The sensitivities to the other atmospheric variables were generally an order of magnitude less. In the plots on the right hand side of the figures the sensitivities to the surface parameters ( $T_g$ ,  $u$ , and  $v$ ) are shown. The sensitivities to  $T_g$  are much larger than the sensitivities to  $u$  and  $v$ , and in most cases are greater than the sensitivities to any of the atmospheric variables.

Positive sensitivities indicate that an increase in the variable will lead to an increase in the  $T_b$ , while a negative sensitivity will result in a reduced  $T_b$  if the variable is increased. The sensitivities to  $T$  and  $T_g$  are primarily positive, meaning that under these conditions an increase in the air or ground temperature will generally lead to an increased  $T_b$ . However, there are small negative sensitivities to  $T$  that are located near the surface in cloudy conditions, which means that an increase in the air temperature actually leads to a decrease in the  $T_b$ .

The sensitivities to  $q$  (in clear and cloudy conditions) and to  $q_c$  in cloudy conditions are both positive and greatest in the lower levels of the atmosphere where their concentrations are greatest. Increases in  $q$  and  $q_c$  lead to increased absorption and emission by the liquid droplets in the atmosphere, which emit more microwave radiation than the ocean surface leading to an increased  $T_b$ . The sensitivity to  $q_s$  is negative and has its greatest magnitude in the upper atmosphere where the  $q_s$  concentration is largest. Microwave radiation is scattered by ice crystals

which results in a smaller  $T_b$  when the  $q_s$  concentration increases. The sensitivities to  $q_r$  (not shown) are mostly positive at 19 and 37 GHz which means the raindrops are emitting radiation. At 85 GHz the sensitivities to  $q_r$  are mostly negative which means that the rain drops are scattering radiation at this frequency.

For the 19H channel (Figure 4) the largest averaged sensitivity of the  $T_b$  to any variable is to  $T_g$  in all weather conditions, although in rainy conditions the sensitivity to  $T$  around 700 mb is almost as large as the sensitivity to  $T_g$ . The same is also true for the 19V channel (Figure 5), although the ratio of the sensitivity to  $T_g$  with the sensitivity to any other variable is much greater in clear and cloudy sky conditions than it is for the 19H channel. The same patterns are seen in the 22 and 37 GHz channels (figures omitted), where the greatest sensitivity is to  $T_g$ , and for the 37 GHz channels the vertically polarized channel has a larger ratio of the sensitivity to  $T_g$  to the sensitivity of any other variable when compared to the horizontally polarized channel.

The sensitivity results also show that 19V  $T_b$ s are less sensitive to the surface wind speed than are the 19H  $T_b$ s (Figures 4 and 5). This was also seen in the 37 and 85 GHz channels. This sensitivity of the model is consistent with observations (Hollinger 1971, Swift 1974) that show horizontally polarized microwave radiation being more sensitive to ocean surface wind speeds than vertically polarized microwave radiation.

For the 85 GHz channels, the sensitivity is again largest for the ground temperature in clear and cloudy sky conditions (Figure 6). However, in rainy conditions, the magnitude of the sensitivities to the air temperature and to the snow ice concentrations are both greater than the sensitivity to the ground temperature. The greatest sensitivities to the air temperature are also located higher in the atmosphere than they are for the other channels, where the ice concentrations are greatest. Also, the ratio of the magnitude of the sensitivity to  $q_s$  to the

magnitude of the sensitivity to any other variable is considerably greater for the 85 GHz channels than it is for any of the other channels.

$T_b$ s are thought to also be largely sensitive to liquid precipitation, especially for the lower channels (19V/H and 37V/H), but the sensitivities to  $q_r$  in rainy conditions are much smaller than the sensitivities to  $T$ . However, the variability in the  $q_r$  fields is much larger than in the  $T$  fields. Therefore, a realistic change in  $q_r$  (of the order of 100 %) could produce as much or more of a change in the  $T_b$  than could a realistic change in the  $T$  field (of the order of only a few percent). The same is also true for the other hydrometeor fields. Even though the sensitivities to these fields are smaller than the sensitivity to  $T$ , realistic changes in these variables can create larger changes in the  $T_b$  than can realistic changes in  $T$ .

The sensitivities of the model are largely what would be expected from physical understanding of radiative transfer in the atmosphere. Therefore, this model is well representing those characteristics of radiative transfer and is an adequate observation operator to be used in a data assimilation scheme.

## 5 Error Characteristics of SSM/I Observations and the Radiative Transfer Model

In order to assimilate  $T_b$ s in a variational scheme, the statistical characteristics of the errors associated with the actual radiance observations (observation errors) as well as the errors which occur when mapping conventional meteorological variables to  $T_b$  space (model errors) need to be known. In this section, we will first investigate the errors associated with SSM/I radiance observations by calculating the structure functions for these values. Then we will focus on the errors which arise from 4-stream approximation in the RTM calculations for a selected

sample of atmospheric profiles and surface conditions. However, the error associated with this approximation is not the only and probably not the largest error associated with RTM. Other sources of error in the RTM will also be discussed.

## 5.1 Observational Errors

Previous studies (Phalippou 1996; Aonashi and Liu 1999) have assumed that SSM/I radiance observations are unbiased and that the radiometric sensitivities of the SSM/I can be used as estimates of the RMS error of the observations. Here, the observations will be assumed unbiased; however, structure functions will be utilized to determine new estimates of the RMS errors of SSM/I observations for each channel.

The structure function for SSM/I  $T_b$ s is defined as (Gandin 1963; Hillger and Vonder Haar 1979)

$$b(\rho_k) = \frac{\sum_{i,j:i>j}^{\rho_k < \rho < \rho_{k+1}} [T_b(\mathbf{r}_i) - T_b(\mathbf{r}_j)]^2}{\sum_{i,j:i>j}^{\rho_k < \rho < \rho_{k+1}} 1}. \quad (8)$$

where an average value of the structure function  $b$  is calculated for each separation distance interval ( $\rho_k$ ) for all pairs of points  $\mathbf{r}_i$  and  $\mathbf{r}_j$  separated by a distance within the interval. The above expression assumes that the field of  $T_b$  deviations from a spatial average is both homogeneous and isotropic so that  $b$  can be expressed as a function of separation distance  $\rho$ .

Gandin (1963) showed that the uncertainty in the measurement can be estimated using the following formula

$$b^*(\rho) = b(\rho) + 2\sigma^2, \quad (9)$$

where  $b^*(\rho)$  is the structure function calculated from actual observations which contain random errors. The variance of the random errors in the measurements is expressed as  $\sigma^2$ . When  $\rho$  approaches zero,  $b(0) = 0$  and  $b^*(0) = 2\sigma^2$ . This means that the measurement uncertainty can be estimated by extrapolating the calculated structure function values to a separation distance

of zero. Here, it is assumed that the structure function flattens out as  $\rho$  approaches zero, so that the structure function value calculated at the smallest separation distance (25 km) will be equal to twice the maximum estimate of  $\sigma^2$ .

In calculating the structure functions, much of the procedure of Hillger and Vonder Haar (1979) was followed. The separation distances were grouped into 50 km intervals (1-50 km, 51-100 km, etc.), and the value calculated was set at the middle of the interval (i.e. the first value is set at 25 km). For this study data were not available over the same area for the time period investigated, so different  $10^\circ$  latitude by  $10^\circ$  longitude boxes were chosen for each of 11 days of data over the tropical Atlantic basin (August 19-29 1998). Table 1 lists the areas for each DMSP satellite (F11, F13, and F14) that were chosen for the analysis. Each box was chosen in an effort to maximize the amount of area of the box covered by SSM/I observations. In order to limit the amount of variation in the function values at small distances a rain flag (Colton and Poe 1999) was applied to the data to remove values in areas of precipitation. At each scan position, if the following conditions were met:  $T_{b_{37V}} - T_{b_{37H}} > 50$  K;  $T_{b_{19V}} < T_{b_{37V}}$ ;  $T_{b_{19H}} < 185$  K; and  $T_{b_{37H}} < 210$ K, then the  $T_b$ s were kept in the analysis, otherwise they were removed.

Figure 7 shows the structure functions for each channel and for each of the three satellites. The structure functions show similar patterns for each satellite, but the values at larger separation distances show a great deal of variation between satellites. The values differed by as much as  $50 \text{ K}^2$  for the horizontally polarized channels. In order to determine the validity of the values calculated, the same procedure using only the first five days of data was repeated. The patterns were similar to those seen in Figure 7.

The basic pattern seen in the structure functions is that the vertically polarized channels (except 22V) show much less structure than the other channels (the horizontally polarized channels and the 22V channel). By removing areas of precipitation from the analysis, areas of

large variability of the  $T_b$  in the 19V, 37V, and 85V channels are also removed because of the large sensitivity of these channels to the atmospheric temperature and snow ice concentrations in rainy areas (Section 4). On the other hand, the 22V channel is sensitive to water vapor, and areas of varying water vapor concentration remain after the rain flag has been applied to the data, which explains why the structure functions are much greater for the 22V channel than they are for the 19V, 37V, and 85V channel. Furthermore, the horizontally polarized channels are more sensitive to surface wind speeds and atmospheric variables while the vertically polarized channels are most sensitive to the ground temperature. This leads to more structure in the horizontally polarized channels (19H, 37H, and 85H) than in the vertically polarized channels (19V, 37V, 85V).

Estimates of  $\sigma$  are given in Table 2 as well as the radiometric sensitivity provided by the manufacturer (last column, from Colton and Poe 1999). As mentioned above, the estimates were also computed for only the first five days of data, and were close to the values calculated (within 20%) when all 11 days of data were utilized. Overall, the estimated values are slightly larger than the radiometric sensitivities. In addition, the estimates changed very little between satellites, except for the 22V and 37V channels of the F11 satellite which differed by more than 1 K from the F13 and F14 satellites. Those channels which have smallest structure function values of (19V, 37V, 85V), also have relatively smaller estimates of the uncertainty of the measurement. Also, these estimates have been made by assuming that the structure function becomes flat at the smallest separation distance, when in actuality it most likely decreases, which would further reduce the estimates. The differences between these estimates and the radiometric sensitivities can also be attributed to the variability caused by the surface wind speed, the water vapor gradients, and possibly by areas of precipitation which were not removed by the rain flag. In Hillger and Vonder Haar (1979) those channels which were sensitive to surface

conditions and water vapor gave estimates of the error which were larger than the manufacturer specified sensitivity. Therefore, SSM/I observation errors are well represented by the radiometric sensitivities of the instrument.

## 5.2 Errors in the RTM

The errors associated with  $T_b$  observations have been discussed; however, the errors associated with the observation operator must also be considered because of large differences between the observed and calculated  $T_{bs}$  (Section 3.3) caused by the errors in the RTM. The ideal situation for assessing the errors associated with the RTM would be to compare observed  $T_{bs}$  with  $T_{bs}$  calculated from the RTM using conventional meteorological observations, such as radiosonde data, as input to the RTM, as was done in Eyre (1992). Unfortunately there are very few conventional observations over oceans where hurricanes are located and the RTM used in this study requires more than just conventional observations as input, namely, cloud/rain water and cloud/snow ice are also needed. Therefore, NWP model fields are used as input to the RTM. However, observed  $T_{bs}$  cannot be used to assess the errors of the RTM because the errors will also include errors associated with the NWP model fields. This especially becomes a problem in rainy areas where it is difficult to ascertain the true atmospheric state. Differences between observed  $T_{bs}$  and those calculated from the RTM can be greater than 100 K in these areas (Section 3.3). Instead, the results of the simplified RTM will be compared with a more complicated and accurate RTM, as was done in Zou et al. (2002) for GPS/MET bending angle data. Here  $T_{bs}$  calculated from the 4-stream RTM are compared with the results from a 32-stream RTM to determine both the bias and the error variance of the 4-stream RTM. Therefore, only the error associated with the differences between the 32 and 4-stream models is being estimated. The differences in the two models are that the 4-stream RTM determines the scattering source term

using a 4-stream discrete ordinate solution and a Henyey-Greenstein scattering phase function (cross polarization scattering is neglected) while the 32-stream RTM determines the scattering source term using a 32-stream discrete ordinate solution and a Mie scattering phase function (Liu 1998).

### 5.2.1 Bias

As mentioned in Section 2, the relatively few number of streams in the 4-stream RTM does not fully account for the amount of radiation that is being scattered, meaning that 4-stream  $T_b$ s,  $T_b^{(4)}$ , will generally be less than  $T_b$ s computed from a RTM with a higher stream number,  $T_b^{(32)}$ . Figure 8 shows the difference between the 32-stream and 4-stream calculated  $T_b$ s ( $T_{b_{85V}}^{(32)} - T_{b_{85V}}^{(4)}$ ). The 12 hr MM5 forecast ending 0000 UTC August 24 was used as input for both RTMs. There are two areas where the differences are significant ( $|T_{b_{85V}}^{(32)} - T_{b_{85V}}^{(4)}| > 0.5$  K). Both of these areas coincide with the areas of maximum integrated rain water in Figure 9. The situation is similar for the other channels as well; in areas of high integrated rain water and snow ice, the 4-stream model consistently under-predicts  $T_b$ s.

Eyre (1992) proposed a method for removing biases in calculated radiances that was partly air-mass dependent (i.e. for different atmospheric conditions, different bias values were removed from the data). The same approach is undertaken here. The differences between the 32-stream and 4-stream RTMs were calculated at each grid point over a 69x69 grid for four different time periods (1200 UTC 22, 1200 UTC 23, 1200 UTC 24, and 1200 UTC 25 August). The bias in rainy areas was then determined by taking the average of all differences at grid points where the integrated rain water was greater than 1.0 mm and/or the integrated snow ice exceeded 0.5 mm. The values of these thresholds were obtained by noting that areas of large  $T_b$  differences were outlined by contours of the integrated rain water and snow ice thresholds. At all other

grid points the bias was considered negligible (the average difference between the RTMs was less than 0.05 K for every channel). The bias corrections to be added to 4-stream  $T_b$ s in rainy areas are given in Table 3.

The bias corrections in Table 3 were then added to the 4-stream  $T_b$ s calculated from an independent 12 hr MM5 forecast ending at 0000 UTC 24 August (these  $T_b$ s were not used in the calculation of the bias correction). The difference between the 32-stream and the corrected 4-stream  $T_b$ s are shown in Figure 10 (this figure can be compared with Figure 8 to see the effects of the bias correction). Overall, the negative bias of the 4-stream model has been reduced. The absolute difference has generally been reduced to less than 1 K. However, in a small area near 24°N 71°W, the integrated rain water and snow ice thresholds were too large so that the bias correction was not applied in an area of relatively large bias. A number of bias estimates were calculated using different combinations of the time periods available. In each case the estimate for each channel varied by less than 0.1 K from the values listed in Table 3.

### 5.2.2 Variance

Aonashi and Liu (1999) estimated the RMS errors of the 4-stream RTM to be 5 K for the 85 GHz channels and 3 K for the other channels based on the results of Liu (1998). However, the results from the bias correction suggest that these estimates might be too high, especially once the bias has been removed. The RMS errors of the bias-corrected 4-stream  $T_b$ s were calculated for the three time periods not used in the bias correction calculations (0000 UTC 23, 0000 UTC 24, and 0000 UTC 25 August). The results are given in Table 4.

The RMS errors were calculated for all grid points and then separately in rainy and non-rainy areas. The rainy and non-rainy areas were defined using the threshold integrated rain water and

snow ice values from above. The RMS errors were also calculated in the rainy areas without removing the bias. Those values are listed in the last column of Table 4.

The RMS errors in rainy areas of the uncorrected  $T_b$ s are slightly larger than the bias estimates, showing that much of the error in the 4-stream model can be attributed to the bias. However, even with the biases removed from the 4-stream  $T_b$ s, the RMS errors are greater in rainy areas than they are in non-rainy areas. The estimated RMS errors for all grid points are closer to the values of the non-rainy RMS errors than they are to the rainy RMS errors, mainly because there are many more non-rainy points than rainy points used in the calculation (13,587 non-rainy points versus 285 rainy points). These results indicate that separate estimates of the error variances should be considered for both rainy and non-rainy areas, or the estimate for the rainy RMS error could be used as a maximum estimate of the RMS error for all areas.

### 5.2.3 Other Error Sources

There are two other potentially large sources of error which arise in rainy conditions that were eluded to in Section 3.3. One source of error results from the plane-parallel assumption in the RTM. The RTM assumes that the NWP fields are horizontally homogeneous over the model grid. In actuality, fields such as rainfall can be highly variable over model grids which can lead to large differences between observed and calculated  $T_b$ s. These differences have been estimated to be on the order of 10's of K (Kummerow et al. 1996).

Another possibly large source of error is due to assumptions made on the particle size distributions for both rain and snow. The RTM assumes that both precipitating liquid and ice are spherical and follow Marshall-Palmer distributions. McKague et al. (1998) estimated the RMS error in the 19 GHz  $T_b$  to be 4.9 K when the rainfall was assumed to follow a Marshall-Palmer distribution. We are unaware of any studies which have estimated the error associated

with assuming a Marshall-Palmer distribution for ice particles, but it is expected that these errors would be larger than errors associated with rainfall and would be greatest for the 85 GHz channels.

The two errors discussed above are likely to be correlated between channels and in space meaning that the forward model (RTM) error covariance matrix would be non-diagonal. Assimilation schemes usually make use of simplifying assumptions, such as the spatial errors are homogeneous and isotropic, in order to reduce the burden of computing full error covariance matrices. The same approach would likely be needed to assimilate microwave  $T_b$ s in rainy environments because some information from the off-diagonal elements is necessary for the assimilation scheme to distinguish between differences due to errors in the model fields and those due to the uncertainty in the RTM, but it would be too cumbersome to compute the entire error covariance matrix and its inverse.

## 6 Summary

Some of the many considerations that must be dealt with when assimilating indirect observations into a NWP model have been discussed in this work. The tangent linear and adjoint RTMs were developed so that the gradient of  $T_b$ s with respect to conventional meteorological variables can be calculated efficiently. These models were shown to give correct results for a selected sample of atmospheric and surface conditions. In formulating these models, a 4-stream RTM was chosen as the observation operator because of its ability to estimate  $T_b$ s in all types of weather, including rain, and its speed in computation. An adjoint sensitivity analysis showed that the 4-stream RTM represents the process of radiative transfer in the atmosphere well.

Estimates of the errors associated with  $T_b$ s were also calculated. The observational error was found to be in line with values that had been used in previous studies. The bias of the

4-stream RTM was estimated based on the type of weather (rainy versus not rainy). With the bias removed, the estimated error variance associated with the 4-stream approximation was found to be much smaller than that found in previous studies.

The results of this work will be used in future studies to directly assimilate SSM/I radiances into NWP forecasts. However, there are still some considerations which must be addressed. As was shown in this study,  $T_b$ s are sensitive to hydrometeor concentrations, and the differences between observed  $T_b$ s and those calculated from model fields are still quite large in rainy areas. Therefore, it is important to have an accurate depiction of the hydrometeor concentrations in order to assimilate  $T_b$ s in the middle of the hurricane. In work planned for the future,  $T_b$  observations will be used to evaluate the performance of different microphysical schemes used in NWP. Also, sensitivity analyses will be conducted for some of these schemes to determine which parameters most influence the calculation of hydrometeor concentrations. Hopefully, once these tasks have been completed the actual impact of the assimilation of  $T_b$ s in hurricane prediction can be investigated.

## Acknowledgments

This work was funded by the Office of Naval Research under grants N0014-99-1-0022 and N-0014-01-0375. The authors would like to thank Dr. Guosheng Liu for providing the codes for the forward 4-stream and 32-stream RTMs and also Mr. Jeffery Hawkins for providing the SSM/I observations used in this study. The authors would also like to express their thanks to three anonymous reviewers whose useful comments have greatly improved this manuscript.

## REFERENCES

- Aonashi, K., and G. Liu, 1999: Direct assimilation of multichannel microwave brightness temperatures and impact on mesoscale numerical weather prediction over the TOGA COARE domain. *J. Met. Soc. Jap.*, **77**, 771-794.
- Colton, M. and G. Poe, 1999: Intersensor Calibration of DMSP SSM/I's: F-8 to F-14, 1987-1997. *IEEE Trans. Geosci. Remote Sensing*, **37**, 418-439.
- Dudhia, J., 1993: A nonhydrostatic version of the Penn State-NCAR Mesoscale Model: Validation tests and simulation of an Atlantic cyclone and cold front. *Mon. Wea. Rev.*, **121**, 1493-1513.
- Eyre, J., 1992: A bias correction scheme for simulated TOVS brightness temperatures. *ECMWF Tech Memo* **186**. 27 pp.
- Eyre, J., G. Kelly, A. McNally, E. Anderson, and A. Persson, 1993: Assimilation of TOVS radiance information through one-dimensional variational analysis. *Q. J. R. Met. Soc.*, **119**, 1427-1463.
- Gandin, L., 1963: *Objective analysis of meteorological fields*. Translated from Russian, Israel Program for Scientific Translations, Jerusalem, 242 pp.
- Hillger, D. W., and T. H. Vonder Haar, 1979: An analysis of satellite infrared soundings at the mesoscale using statistical structure and correlation functions. *J. Atmos. Sci.*, **36**, 287-305.
- Hollinger, J., R., 1971: Passive microwave measurements of the sea surface. *IEEE Trans. Geo. Sci. Electron.*, **91**, 165-169.
- Hollinger, J., R. Lo, G. Poe, and R. Savage, J. Pierce, 1987: Special sensor microwave/imager user's guide. Naval Research Laboratory, Washington, D.C. 177 pp.
- Hollinger, J., 1991: DMSP special sensor microwave/imager. Calibration/Validation. Naval Research Laboratory, Washington, D.C. 89 pp.

- Kummerow, C., W.S. Olson, and L. Giglio, 1996: A simplified scheme for obtaining precipitation and vertical hydrometeor profiles from passive microwave sensors. *IEEE Trans. Geosci. Remote Sensing*, **34**, 1213-1232.
- Le Dimet, F., and O. Talagrand, 1986: Variational algorithms for analysis and assimilation of meteorological observations: theoretical aspects. *Tellus*, **38A**, 97-110.
- Liou, K.-N., 1974: Analytic two-stream and four-stream solutions for radiative transfer. *J. Atmos. Sci.*, **31**, 1473-1475.
- Liu, G., 1998: A fast and accurate model for microwave radiance calculations. *J. Met. Soc. Jap.*, **76**, 335-343.
- McKague, D., K. F. Evans, and S. Avery, 1998: Assessment of the effects of drop size distribution variations retrieved from UHF radar on passive microwave remote sensing of precipitation. *J. App. Met.*, **37**, 155-165.
- Phalippou, L., 1996: A variational retrieval of humidity profile, wind speed and cloud liquid-water path with the SSM/I: Potential for numerical weather prediction. *Q. J. R. Met. Soc.*, **122**, 327-355.
- Swift, C. T., 1974: Microwave radiometer measurements of the cape cod canal. *Radio Sci.*, **9**, 641-653.
- Wentz, F., 1991: User's manual SSM/I antenna temperature tapes, revision 1. *RSS Technical Report*, 120191, Remote Sensing Systems, Santa Rosa, CA, 50 pp.
- Zou, X., A. Barcilon, I. Navon, J. Whitaker, and D. Cacuci, 1993: An adjoint sensitivity study of blocking in a two-layer isentropic model. *Mon. Wea. Rev.*, **121**, 2833-2857.
- Zou, X., F. Vandenberghe, M. De Pondeva, and Y.-H. Kuo, 1997: Introduction to adjoint techniques and the MM5 adjoint modeling system. *NCAR Technical Note*, NCAR/TN-435-STR, 122 pp.

- Zou, X., and Q. Xiao, 2000: Studies on the initialization and simulation of a mature hurricane using a variational bogus data assimilation scheme. *J. Atmos. Sci.*, **57**, 836-860.
- Zou, X., Q. Xiao, A. Lipton, and G. Modica, 2001: A numerical study of the effect of GOES sounder cloud-cleared brightness temperatures on the prediction of Hurricane Felix. *J. App. Met.*, **40**, 34-55.
- Zou, X., H. Liu, and R. Anthes, 2002: A statistical estimate of errors in the calculation of radio-occultation bending angles caused by a 2D approximation of ray tracing and the assumption of spherical symmetry of the atmosphere. *J. Atmos. Ocean. Tech.*, **19**, 51-64.
- Zupanski, M., 1995: An iterative approximation to the sensitivity in calculus of variations. *J. Atmos. Sci.*, **123**, 3590-3604.

## Table Captions

Table 1: Areas used to calculate the structure functions. (August 19-29 1998)

Table 2: Estimated RMS errors for SSM/I  $T_b$ s. All units in K.

Table 3: Bias corrections for the 4-stream RTM.

Table 4: Estimated RMS errors of the RTM.

## Figure Captions

Figure 1: Observed (left) and calculated (right)  $T_b$ s for the 19V channel at 0000 UTC 25 August 1998. Contoured every 10 K. The center of Bonnie is indicated by the filled circle.

Figure 2: Observed (left) and calculated (right)  $T_b$ s for the 85V channel at 0000 UTC 25 August 1998. Contoured every 10 K in the left hand plot and every 20 K in the right hand plot. The center of Bonnie is indicated by the filled circle.

Figure 3: Averaged profiles of  $q_r$ ,  $q_s$ ,  $q_c$ , and  $q_{ci}$  in (a) clear, (b) cloudy, and (c) rainy conditions, and (d) of  $q$  in all conditions. Horizontal bars represent the standard deviation.

Figure 4: Averaged relative sensitivities for the 19H channel to (a)  $T$  and  $q$  for clear conditions, (b)  $T$  and  $q_s$  for rainy conditions, and (c)  $T$ ,  $q$ , and  $q_c$  for cloudy conditions, and to  $T_g$ ,  $u$ , and  $v$  for (d) clear conditions, (e) rainy conditions, and (f) cloudy conditions.

Figure 5: Same as figure 4 except for the 19V channel.

Figure 6: Same as figure 5 except for the 85V channel.

Figure 7: Structure function for satellite F11 (top), F13 (middle), and F14 (bottom).

Figure 8: Difference between the 32-stream and 4-stream  $T_b$ s for the 85V channel. Contoured at -0.1, 0.1, 0.4, 0.8, 1.2, 1.6, 2.0 K.

Figure 9: 12 hr forecast of integrated rainwater (solid contour every 1.5 mm) and SLP (dashed contour every 4 mb) valid 0000 UTC 24 August 1998.

Figure 10: Difference between the 32-stream and 4-stream  $T_b$ s for the 85V channel after the bias corrections have been added to the 4-stream  $T_b$ s. Contoured at -0.8, -0.4, -0.1, 0.1, 0.4, 0.8, 1.2 K.

Table 1: Areas used to calculate the structure functions. (August 19-29 1998)

Date	F11		F13		F14	
	Lat	Lon	Lat	Lon	Lat	Lon
19th	15-25N	50-60W	25-35N	63-73W	25-35N	50-60W
20th	10-20N	47-57W	20-30N	60-70W	NA	NA
21st	5-15N	45-55W	25-35N	55-65W	15-25N	47-57W
22nd	25-35N	63-73W	20-30N	55-65W	25-35N	65-75W
23rd	20-30N	60-70W	20-30N	50-60W	25-35N	63-73W
24th	20-30N	57-67W	15-25N	50-60W	20-30N	60-70W
25th	20-30N	55-65W	10-20N	47-57W	20-30N	58-68W
26th	20-30N	50-60W	25-35N	65-75W	20-30N	55-65W
27th	15-25N	48-58W	25-35N	63-73W	20-30N	50-60W
28th	10-20N	45-55W	25-35N	60-70W	15-25N	50-60W
29th	25-35N	65-75W	25-35N	57-67W	15-25N	47-57W

Table 2: Estimated RMS errors for SSM/I  $T_b$ s. All units in K.

	F11	F13	F14	Sens.
19V	0.79	0.82	0.80	0.80
19H	1.19	1.16	1.29	0.80
22V	1.22	1.05	2.95	0.80
37V	1.85	0.89	0.91	0.60
37H	1.57	1.54	1.63	0.60
85V	1.82	1.17	1.28	1.10
85V	3.03	2.27	2.63	1.10

Table 3: Bias corrections for the 4-stream RTM

Channel	Correction (K)
19V	0.66
19H	0.75
22V	0.45
37V	0.78
37H	0.85
85V	1.36
85H	1.33

Table 4: Estimated RMS errors of the RTM

Channel	All (K)	Non-Rainy (K)	Rainy (K)	Rainy w/o bias cor. (K)
19V	0.0663	0.0467	0.3318	0.7430
19H	0.0782	0.0667	0.2931	0.8206
22V	0.0377	0.0181	0.2314	0.4846
37V	0.1073	0.0835	0.4782	0.9155
37H	0.1217	0.1108	0.3686	0.9570
85V	0.1305	0.0995	0.5977	1.4519
85H	0.1353	0.0991	0.6503	1.4343

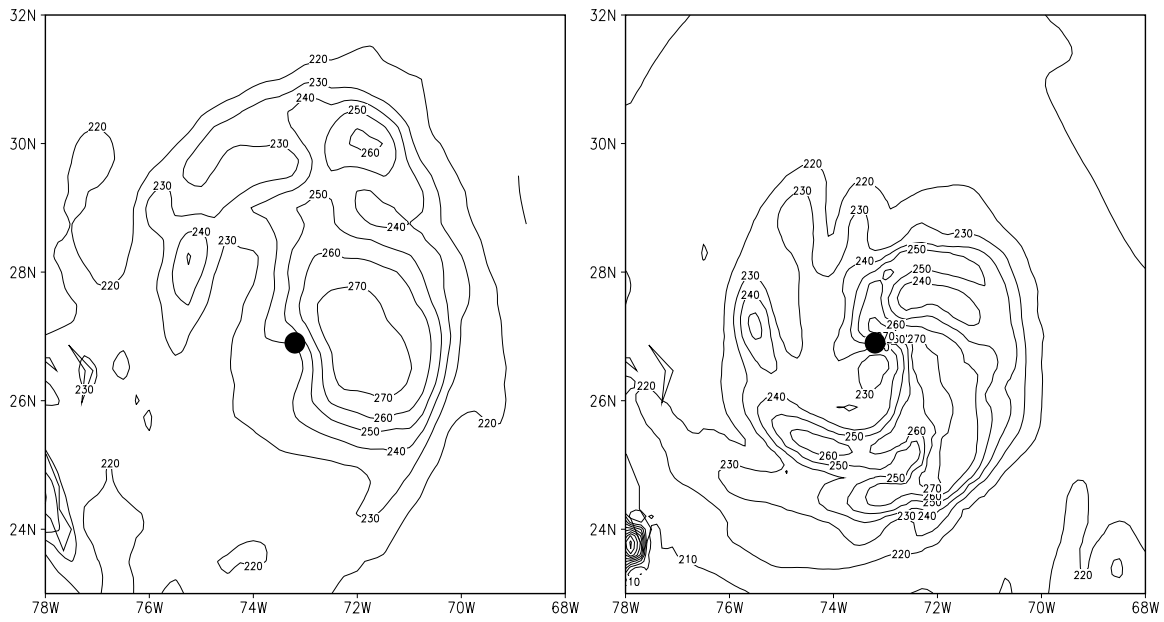


Figure 1: Observed (left) and calculated (right)  $T_b$ s for the 19V channel at 0000 UTC 25 August 1998. Contoured every 10 K. The center of Bonnie is indicated by the filled circle.

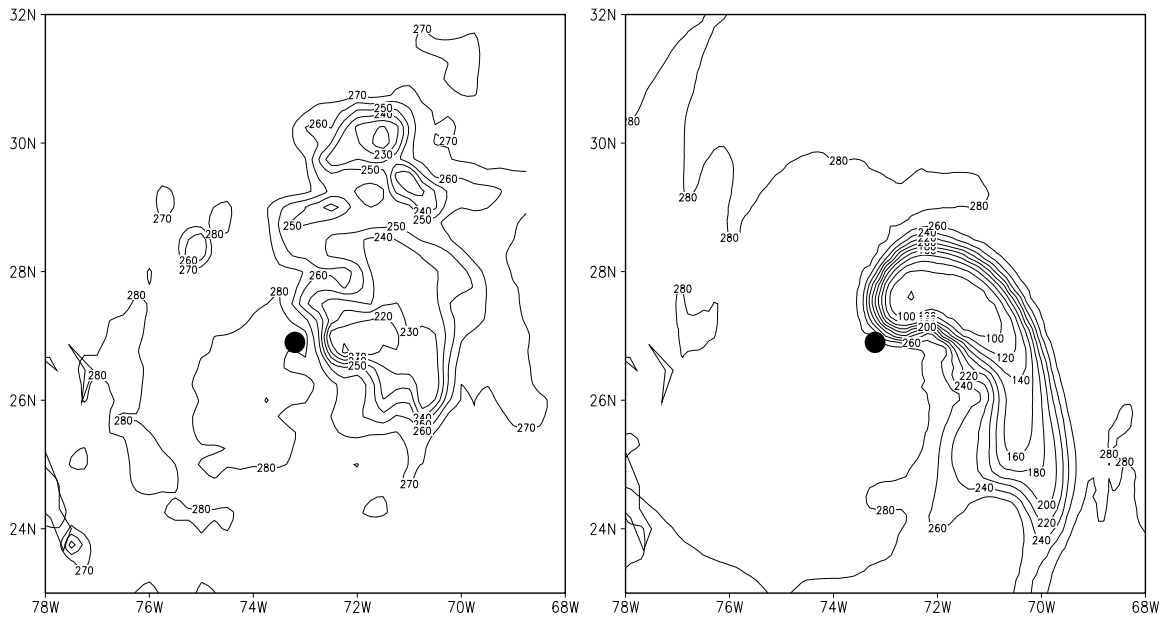


Figure 2: Observed (left) and calculated (right)  $T_b$ s for the 85V channel at 0000 UTC 25 August 1998. Contoured every 10 K in the left hand plot and every 20 K in the right hand plot. The center of Bonnie is indicated by the filled circle.

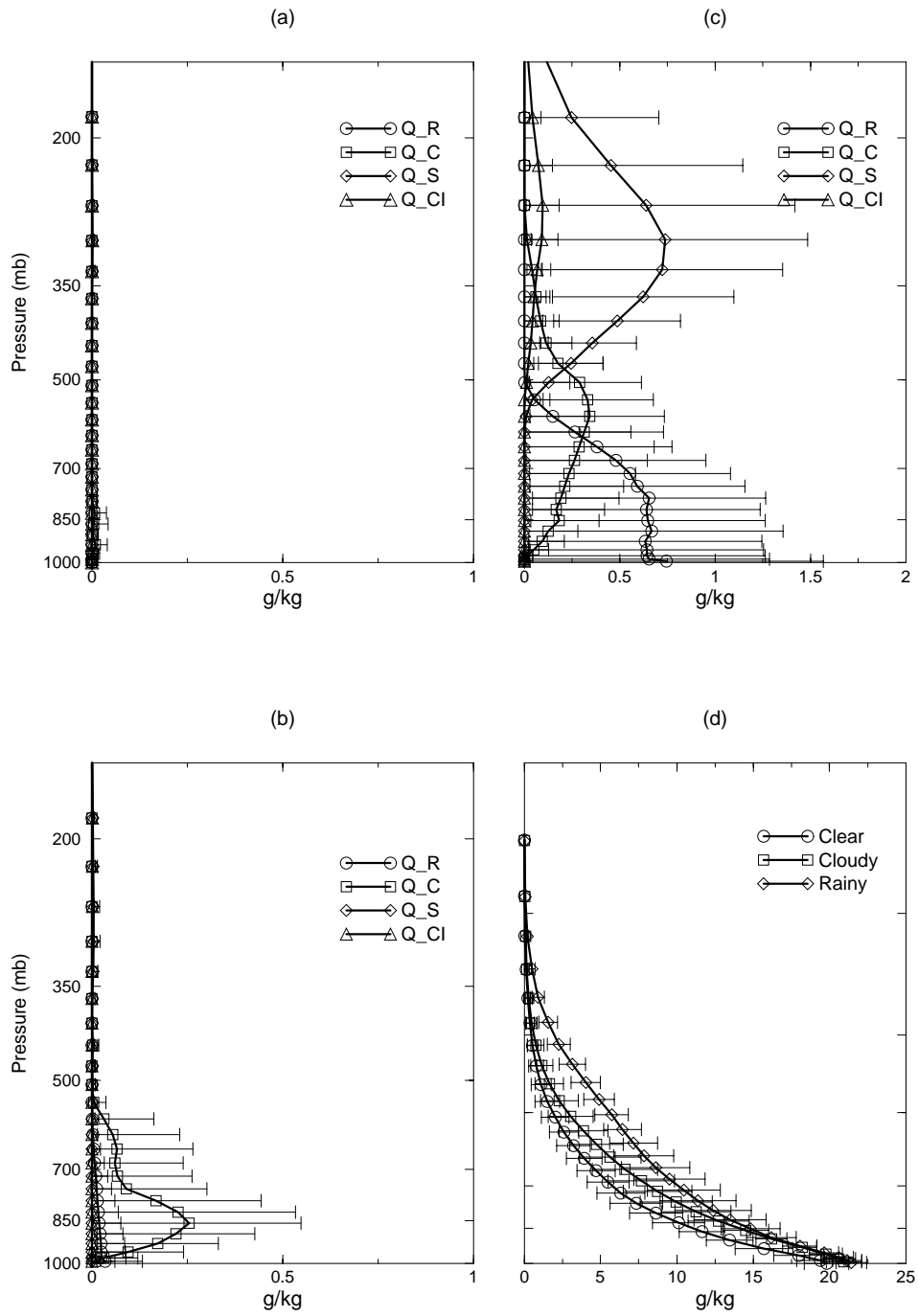


Figure 3: Averaged profiles of  $q_r$ ,  $q_s$ ,  $q_c$ , and  $q_{ci}$  in (a) clear, (b) cloudy, and (c) rainy conditions, and (d) of  $q$  in all conditions. Horizontal bars represent the standard deviation.

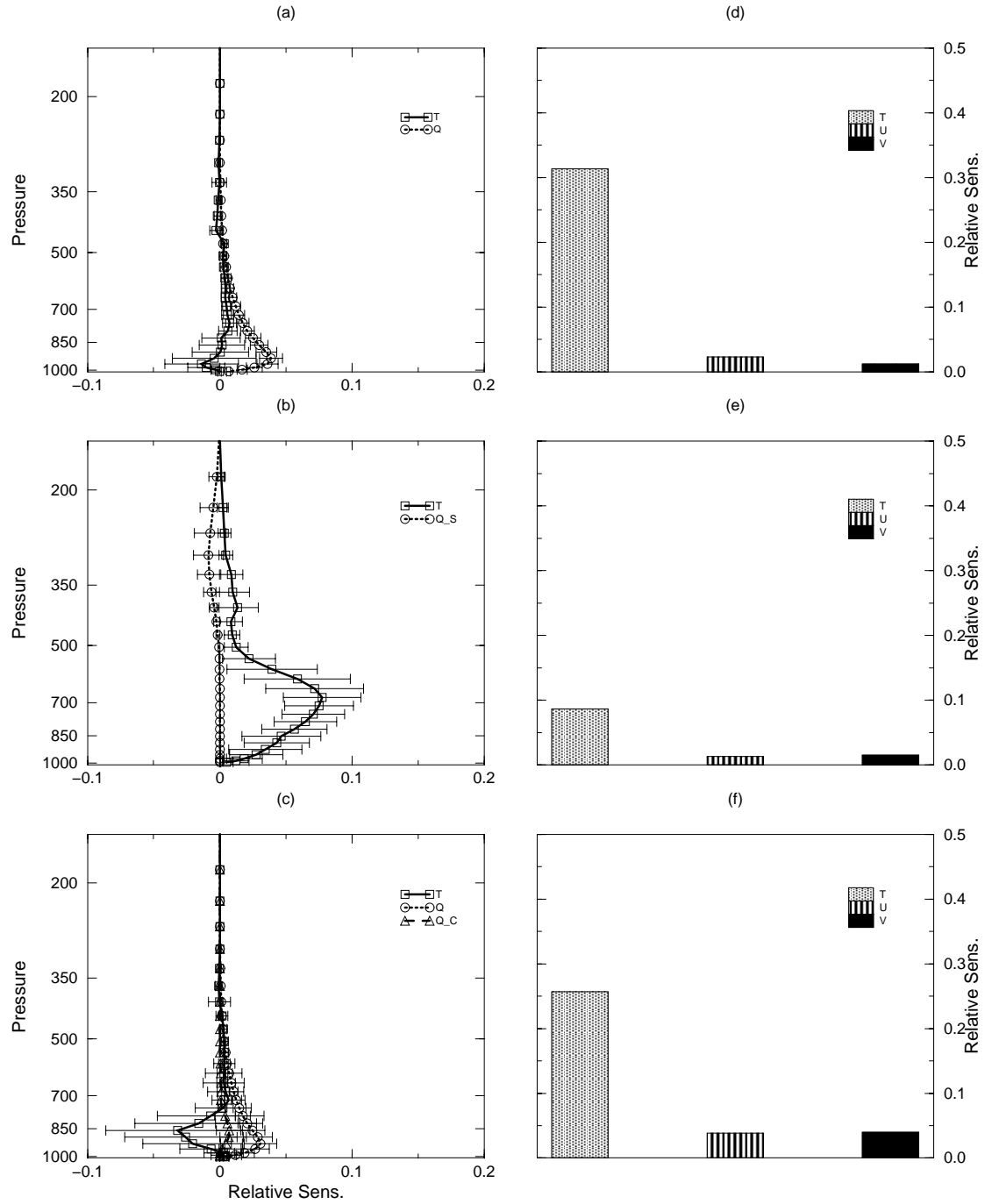


Figure 4: Averaged relative sensitivities for the 19H channel to (a)  $T$  and  $q$  for clear conditions, (b)  $T$  and  $q_s$  for rainy conditions, and (c)  $T$ ,  $q$ , and  $q_c$  for cloudy conditions, and to  $T_g$ ,  $u$ , and  $v$  for (d) clear conditions, (e) rainy conditions, and (f) cloudy conditions.

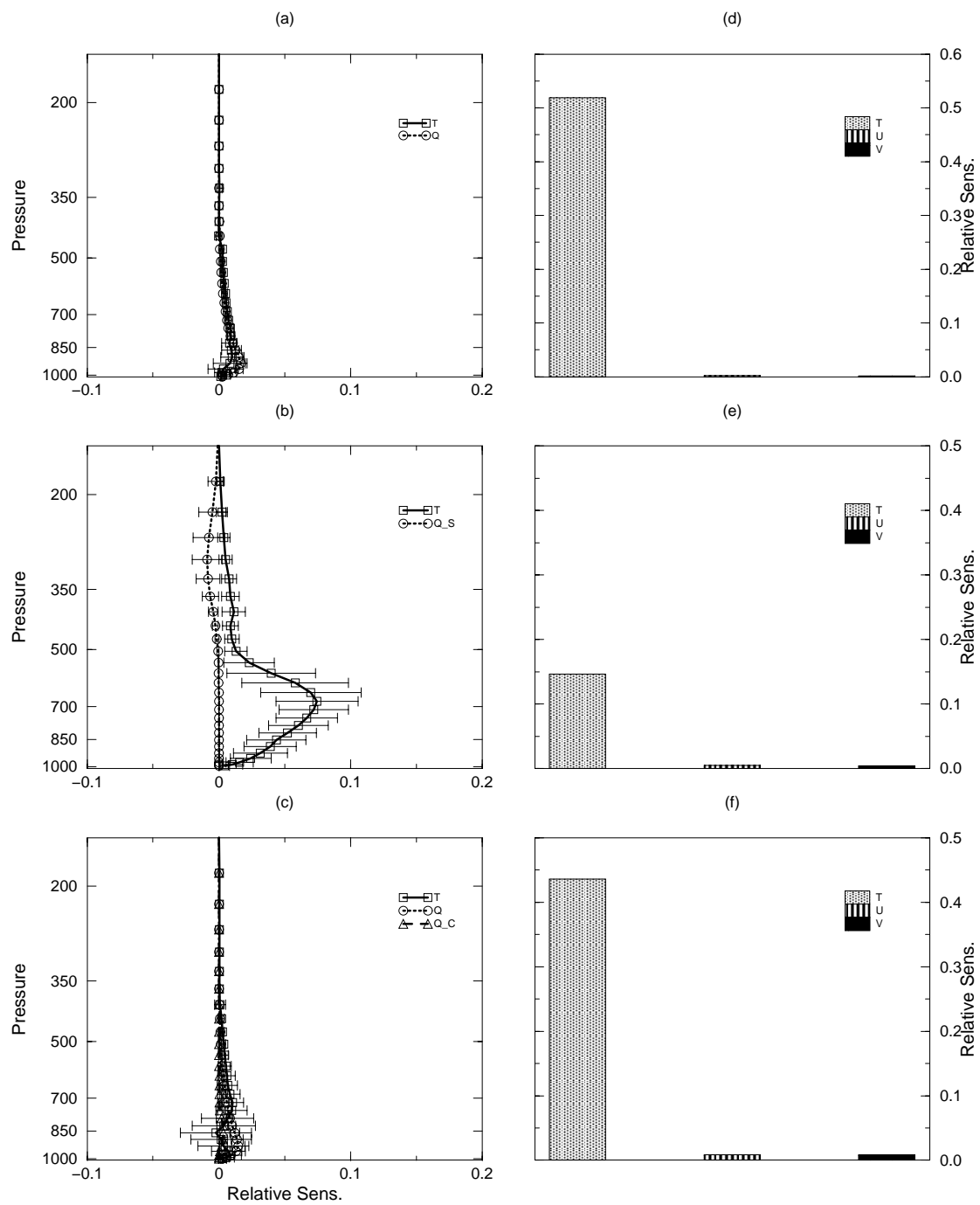


Figure 5: Same as figure 4 except for the 19V channel.

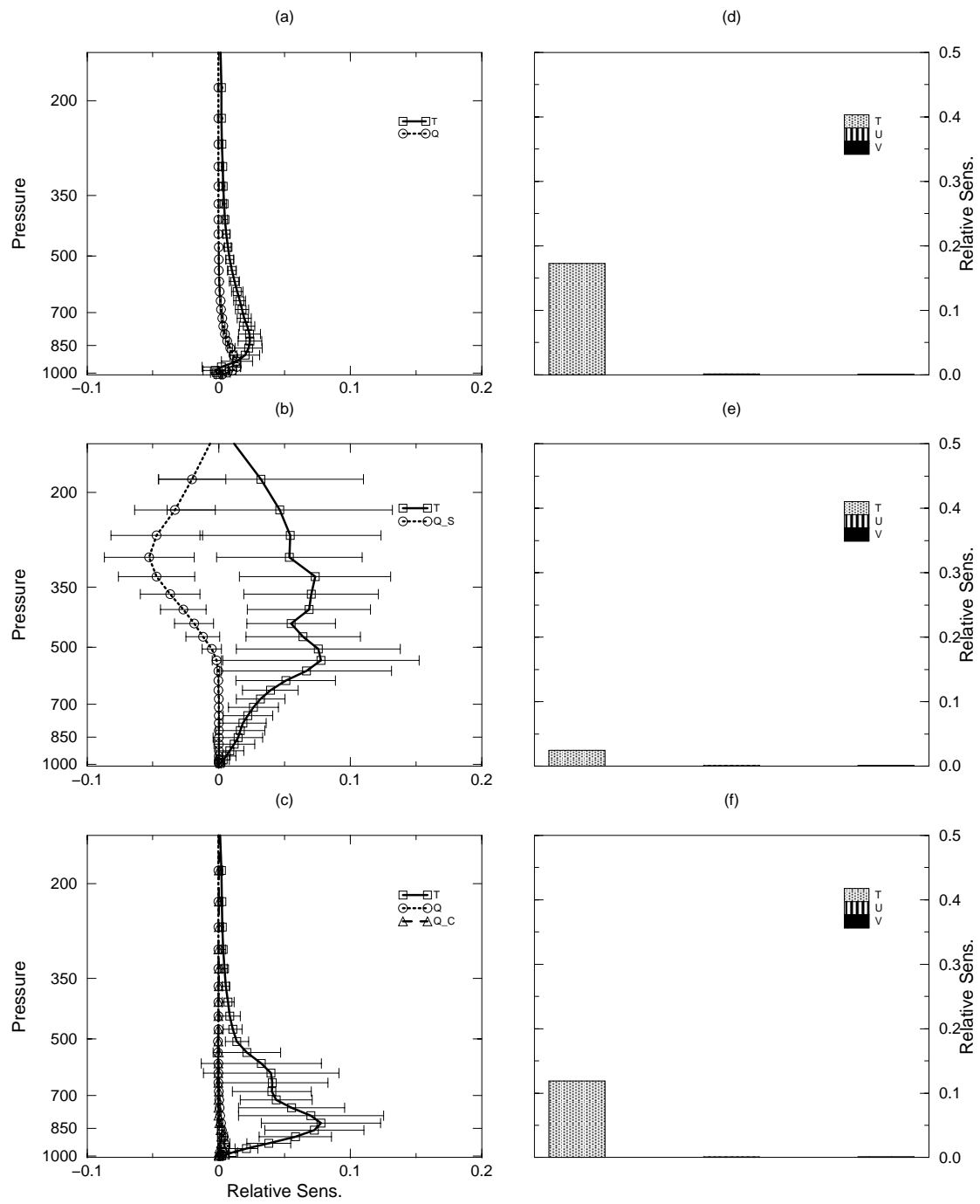


Figure 6: Same as figure 5 except for the 85V channel.

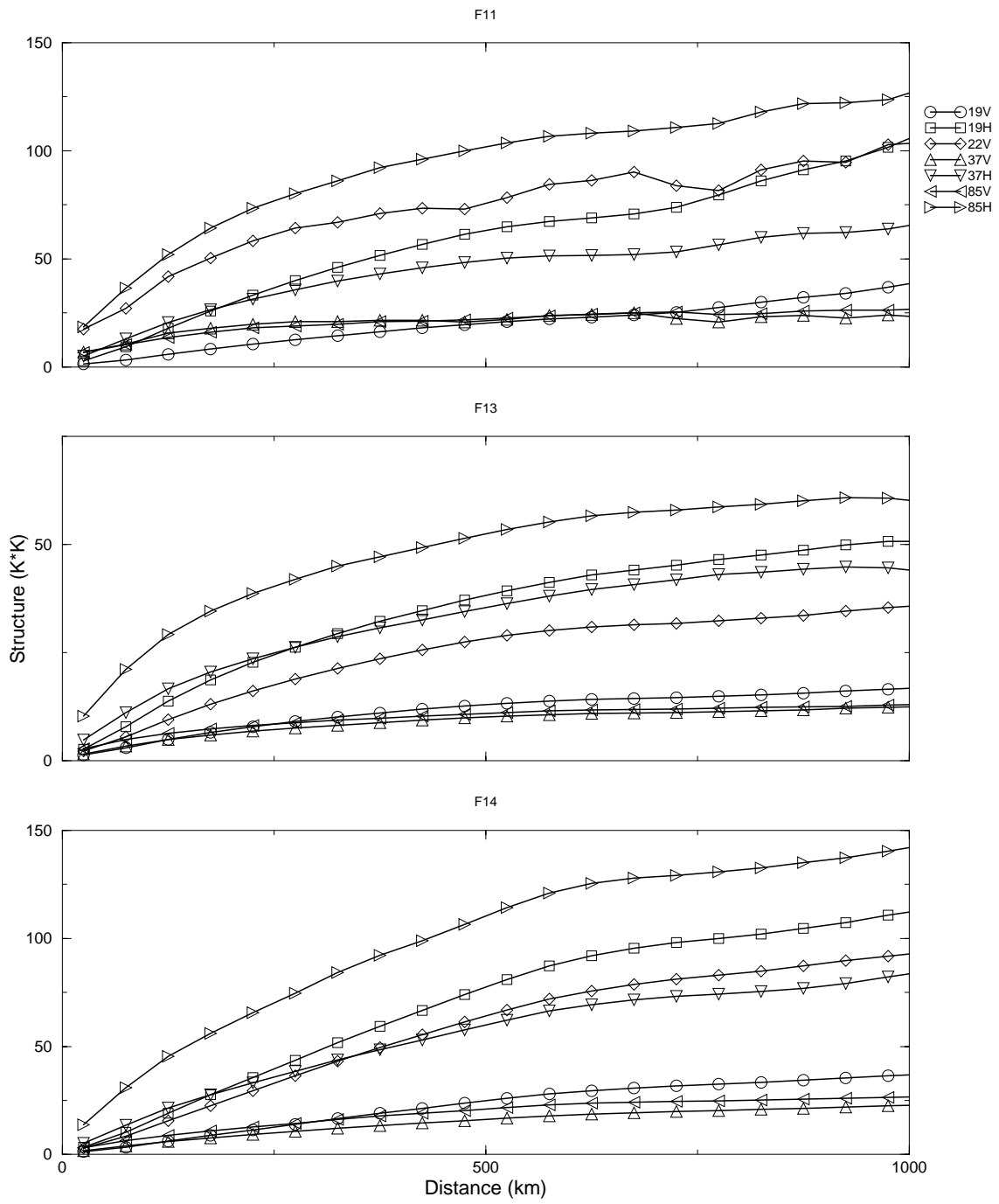


Figure 7: Structure function for satellite F11 (top), F13 (middle), and F14 (bottom).

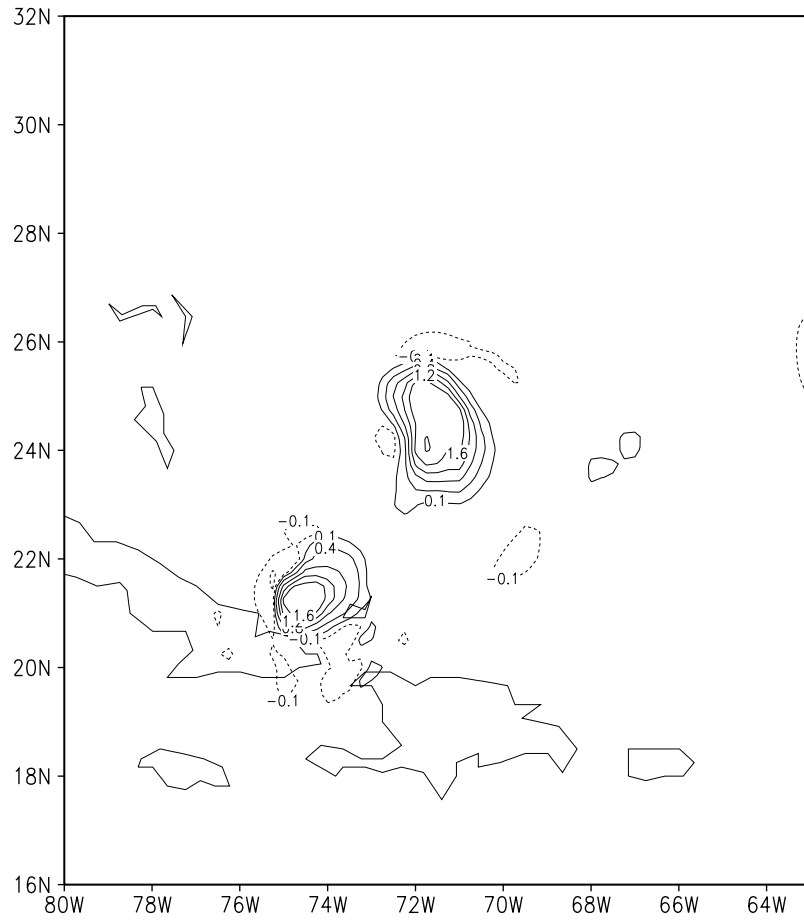


Figure 8: Difference between the 32-stream and 4-stream  $T_b$ s for the 85V channel. Contoured at -0.1, 0.1, 0.4, 0.8, 1.2, 1.6, 2.0 K.

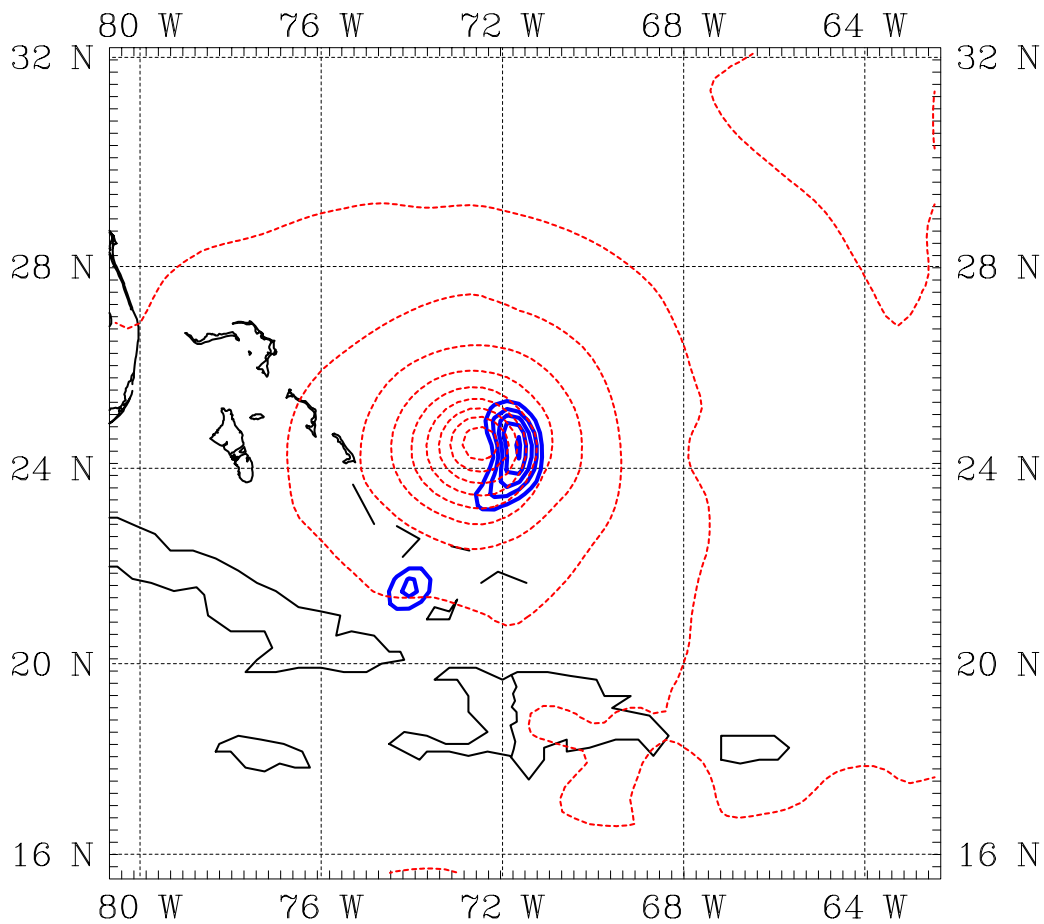


Figure 9: 12 hr forecast of integrated rainwater (solid contour every 1.5 mm) and SLP (dashed contour every 4 mb) valid 0000 UTC 24 August 1998.

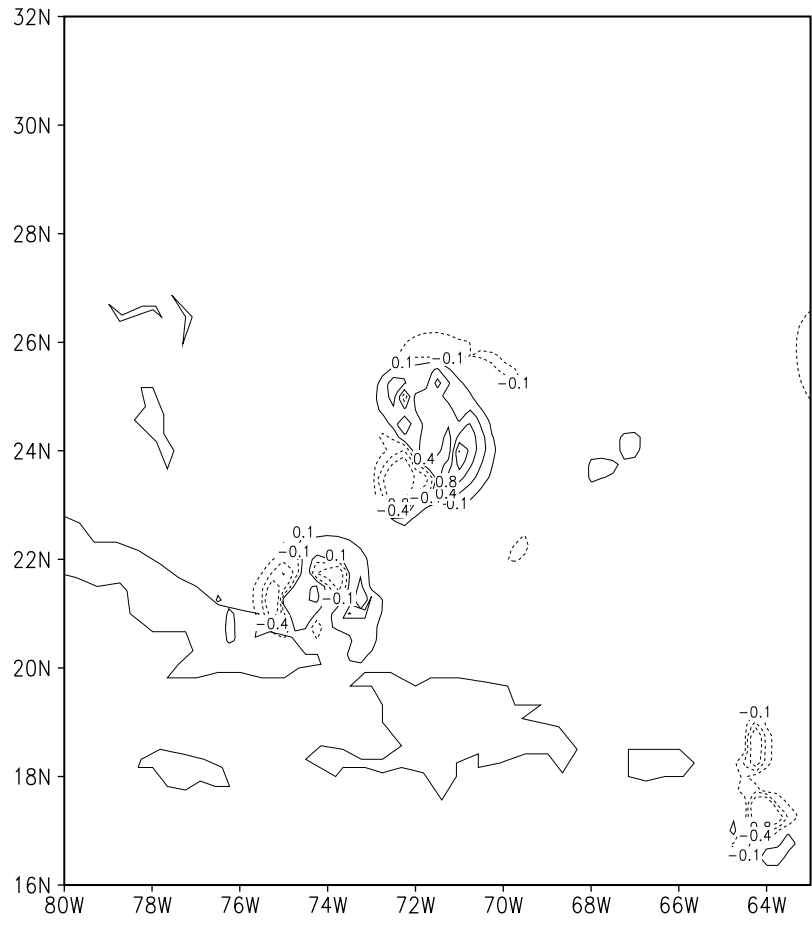


Figure 10: Difference between the 32-stream and 4-stream  $T_b$ s for the 85V channel after the bias corrections have been added to the 4-stream  $T_b$ s. Contoured at -0.8, -0.4, -0.1, 0.1, 0.4, 0.8, 1.2 K.